Planetary and Space Science 137 (2017) 64–72

Contents lists available at ScienceDirect

Planetary and Space Science

journal homepage: www.elsevier.com/locate/pss

# Simulations of stellar winds and planetary bodies: Ionosphere-rich obstacles in a super-Alfvénic flow

Y. Vernisse[a,b,*], J.A. Riousset[c], U. Motschmann[d,e], K.-H. Glassmeier[f,g]

[a] Institut de Recherche en Astrophysique et Planétologie, Toulouse, France
[b] Université Paul Sabatier, Toulouse, France
[c] Embry Riddle Aeronautical University, Daytona Beach, FL, USA
[d] Institute for Theoretical Physics, TU Braunschweig, Braunschweig, Germany
[e] DLR-Institute for Planetary Research, Berlin, Germany
[f] Institute for Geophysics and Extraterrestrial Physics, TU Braunschweig, Braunschweig, Germany
[g] Max Planck Institute for Solar System Research, Göttingen, Germany

ARTICLE INFO

*Keywords:*
Hybrid simulation
Planetary ionosphere
Magnetospheric currents
Unmagnetized body

ABSTRACT

We classify the interactions of planetary obstacles with an upstream stellar wind. The investigation of each type of interaction is made using a three dimensional simulation code based on the hybrid modeling of the interplanetary plasma (the AIKEF code). The aim is to fill up the parameter space of magnetospheric interactions. In this work, we focus on highly resistive obstacles, non-magnetized but possessing an ionosphere. We examine different ionospheric types by focusing on one parameter: the ionospheric production. Two types of ionospheric ions are used: $H^+$ and $O^+$, to show the influence of ionospheric ion mass on the interaction region configuration. The interaction types are classified using an equivalent conductivity of the ionosphere. The resulting induced magnetospheric interactions are described using the currents flowing throughout the interaction region. The essence of the interaction region structure is summarized into three-dimensional diagrams of the current distribution. The results show three main stages of development. The first is a lunar-type interaction with raising asymmetries. The second is depicted by the presence of a growing induced magnetopause and an interaction region which asymmetry depends on the mass of the ionospheric ions. The last stage is a fully developed induced magnetosphere, or Venus-like interaction, with a symmetric magnetosphere.

## 1. Introduction

Unmagnetized obstacles in the Solar System interact with the Solar wind in different manners. Inert and ionosphere-less obstacles (e.g., the Earth moon) generate a wake on the nightside of the interaction region (Whang, 1968). Ionosphere-rich obstacles (e.g., Venus) drag the solar wind and may trigger an induced magnetosphere balancing the solar wind pressure (Bauer et al., 1977; and references therein]. Studies of the solar wind - or any magnetized plasma - directly impinging an ionospheric-rich obstacle were done with Venus, Mars, comets, and several outer moons as Titan and Dione. In such a type of interaction, an induced magnetic field is generated by the encounter of the interplanetary magnetic field (IMF) and the ionosphere, which acts as a super-conducting shell encompassing the planet (Baumjohann et al., 2010). The term induced magnetic field here does not refer to a temporal variation of the IMF (see e.g. Jia et al. (2015)), it refers to a steady state field resulting from various processes. Various ionospheric mechanisms can generate the conditions necessary to trigger an induced field. The pick-up process (e.g. Phillips et al., 1987) consists of a transfer of momentum between the ionosphere and the impinging Solar Wind. It is also named “mass loading” and is the main effect discussed in this study. Collisions play a major role in solar wind interactions physics when the solar wind pressure is high enough to push the ionosphere down to the lower atmosphere. The net effect of collisions is expressed in the so-called Pedersen conductivity tensor (Baumjohann and Treumann, 1996).

Although numerous simulations of the interaction of an inflowing solar wind with planetary ions were performed with dense ionospheres (Venus-type or Mars-type), or weak sputtering and reflected particles (Wurz et al., 2007; Lipatov et al., 2012; Davis et al., 2014; Fatemi et al., 2014), fewer models were performed with different ionization rates. Such models investigating the effect of the production rate are typical for comets which, by approaching or moving away from the sun, are subjected to an extremely variable ion production rate (Cravens et al.,

* Corresponding author at: Institut de Recherche en Astrophysique et Planétologie, Toulouse, France.
*E-mail address:* yoann.vernisse@irap.omp.eu (Y. Vernisse).

http://dx.doi.org/10.1016/j.pss.2017.01.012
Received 12 January 2017; Accepted 26 January 2017
Available online 28 January 2017
0032-0633/ 

1987; Biver et al., 1997, Bagdonat and Motschmann, 2002a; Motschmann and Kührt, 2006). Variations of ionization rates at planetary obstacles may have many causes, either the evolution of the solar system (Kulikov et al., 2007), seasonal effects (Yamauchi et al., 2015), solar cycles (Russell et al., 2006), or complex mechanisms requiring dedicated modeling (Marchaudon and Blelly, 2015). The quantification of the picked up ions is a long-term study implying both modelings and measurements, aiming to a complete description of the involved mechanisms (Curry et al., 2015). General implications of the production rate in ionospheric interactions for non-solar system production rate requires extrapolation but are consistent, owing to the sturdiness of the simulation codes (Johansson et al., 2009; Jarvinen et al., 2009).

Currents in planetary interactions with an impinging magnetized plasma are helpful to provide a self-consistent description of the interaction region. Using the property that currents must close at steady state, exchange between the different regions of the whole interaction becomes easy to illustrate (Mauk and Zanetti, 1987; Siscoe et al., 2000, Siscoe and Siebert, 2006). Complete description of the current systems of unmagnetized airless body are available in the literature (Fatemi et al., 2013; Vernisse et al., 2013; Zhang et al., 2014; Simon, 2015). Currents systems of induced magnetospheres have also been detailed in the literature (Baumjohann et al., 2010). Currents and magnetic field distortions associated with picked up ion are particularly difficult to investigate when multiple species are present in the ionosphere, and simulating one species at a time may help resolve part of that challenge (Jarvinen et al., 2016).

A full coverage of types of interaction between airless unmagnetized bodies and unmagnetized bodies possessing a developed ionosphere remains to do. In this paper, we propose a simple description of the currents in the interaction region of an unmagnetized obstacle with an upstream solar wind, using various production rates. We perform a number of hybrid simulation runs (the AIKEF code, see Mueller et al. (2011)) using $H^+$ and $O^+$ ions for generating the ionosphere, based on a Chapman model. We vary the ionospheric ion production from zero to Venus-like production rate between the simulations and summarize the results in three-dimensional diagram using the major currents flowing in the interaction region. The main driver of the interaction is the mass loading, associated with the pick-up current. When the mass loading is sufficiently high – or the magnetic field induced by the pickup current – an induced magnetosphere builds up and deviates the particles from the planetary surface. Ionospheres based on $H^+$ and $O^+$ diverge mostly at intermediary state, and magnetospheres induced by either ionized hydrogen or ionized oxygen only differ in size by a small percentage.

## 2. Model and methodology

### 2.1. The AIKEF simulation code

The results presented in this paper were produced using AIKEF, based on the hybrid model. It is based on the curvilinear code by Bagdonat and Motschmann (2002b). Subsequent development and details of the simulation code such as the particles merging and splitting process, or boundary conditions are provided in Mueller et al. (2011). Hybrid model simulations are based on three major assumptions: the electrons are considered massless (thus fluid), the displacement current is neglected, and the medium is quasi-neutral. Applied to Maxwell's equations, this leads to the general Ohm's law. The ions motions are individually described by their momentum equation, which consists in the Lorentz force. More details are available in the numerous studies which have successfully treated solar system planets such as Mercury (Mueller et al., 2012; Wang et al., 2010), Venus (Martinecz et al., 2009), Mars (Boesswetter et al., 2004). AIKEF was also used to model satellites such as Enceladus (Kriegel et al., 2009, 2011), Tethys (Simon et al., 2009), Titan (Mueller et al., 2010; Simon et al., 2006), Rhea (Roussos et al., 2008; Simon et al., 2012), the Moon (Wiehle et al., 2011; Wang et al., 2011).

**Table 1**
Normalizations formulas used in our simulations. An example with Earth's typical upstream parameters is provided. The terms $m_p$ and e are the mass of the proton and the elementary charge, respectively. In this paper, $B_0 = B_{IMF}$, $n_0 = n_{sw}$, $q_0 = q_{sw}$, and $m_0 = m_{sw}$ (with $B_{IMF}$, $n_{sw}$, $q_{sw}$, and $m_{sw}$ are the upstream stellar wind magnetic field magnitude, number density, particle charge, and particle mass, respectively), i.e., the normalization is made using the upstream stellar wind parameters. The term $v_{A,0}$ stands for the Alfvén velocity.

| Quantity | Variable | Normalization | Example |
|---|---|---|---|
| Magnetic field | B | $B_0$ | 5.0 nT |
| Number density | n | $n_0$ | 5.0 $cm^{-3}$ |
| Mass | $m_\alpha$ | $m_0$ | 1.0 $m_p$ |
| Charge | $q_\alpha$ | $q_0$ | 1.0 e |
| Time | t | $t_0 = m_0/(q_0 B_0)$ | 2.1 s |
| Length | x | $x_0 = (m_0/\mu_0 q_0^2 n_0))^{1/2}$ | $1{\cdot}10^2$ km |
| Velocity | u | $u_0 = x_0/t_0 = B_0/(\mu_0\rho_0)^{1/2} = v_{A,0}$ | 48 km/s |
| Current density | j | $j_0 = q_0\ n_0\ v_{A,0}$ | 3.9 $nA/m^2$ |
| Electric field | E | $E_0 = v_{A,0}\ B_0$ | $2.4\times10^{-4}$ V/m |
| Resistivity | η | $\eta_0 = E_0/j_0$ | $6.2{\cdot}10^3\ \Omega$ m |
| Pressure | P | $P_0 = B_0^2/(2\ \mu_0)$ | $9.9{\cdot}10^{-3}$ nPa |
| Ion Production rate | Q | $Q_0 = n_0 \times_0^3/t_0$ | $2.9{\cdot}10^{21}\ s^{-1}$ |

The quantities presented in this paper are normalized following Table 1. All quantities (first and second columns) can be formulated using the magnetic field, the number density, the particle charge, and the particle mass. We choose to present the simulation results in normalized quantities to unify all efforts in a self-consistent, non-body-specific approach. We provide a normalization table for any a posteriori comparison (third column of Table 1, with the expressions pertaining to this paper. An illustration of typical parameters at Earth is given in the fourth column of Table 1.

The simulation domain geometry is comparable to that of our earlier study (Vernisse et al., 2013). The upstream plasma flows along the +x-axis and the IMF is oriented along the −z-axis. The resolution of the simulation domain obtained for this work is as follow: the box consists of $400x_0$, where $x_0$ is the ion inertial length (see Table 1 for definition) along each axis, divided into 128 blocks. The center of the obstacle is taken at the origin of the coordinate system, and is situated at the center of the y and z-axis, and at one third of the x-axis. The radius of the obstacle is $20x_0$.

We use a static mesh with two level of refinement. The first level of refinement is a box extending from $-80x_0$ to $+200x_0$ along the x-axis, from $-70x_0$ to $+70x_0$ along the y and z axe. The second level of refinement extends from $-60x_0$ to $+200x_0$ along the x-axis and from $-50x_0$ to $+50x_0$ along the y and z axe. The resolution of the finest cell is about $1\times_0$. A particle splitting and merging procedure is implemented (Mueller et al., 2011) in order to keep a number of 100 particle per cell in average. We note that the finest resolution is sufficient for a correct modeling of the dayside structures of the interaction region such as the bow shock and the plasmapause, which strongly depends on the numerical dissipation in simulations.

The resistivity of the obstacle has been thoroughly discussed in our precedent study (Vernisse et al., 2013). The same resistivity profile has been used in this study. The obstacle is considered as a highly resistive body, but not a perfect insulator.

### 2.2. Ionosphere modeling and parameters

We implement a Chapman profile to model an ionosphere at the surface of the obstacle in our simulations. We do not discuss the technical part of that model which is already well described in the literature (Baumjohann and Treumann, 1996). The Chapman profile can be summarized by its expression, which represents the probability of generating an ion at a point in the spatial domain:

$$q_v(r, \quad \theta) = \kappa_v \sigma_v n_{n,surf} I_\infty exp\left(-\frac{r}{H} - \frac{\sigma_v n_{n,surf} H}{\cos\theta} \exp\left(-\frac{r}{H}\right)\right) \quad , \tag{1}$$

where $q_v$ is the photoionization frequency. The shape of the profile depends on two parameters: H and $\sigma_v n_{n,surf}$, which are the scale heigth of the atmosphere and the density of neutrals at the surface of the obstacle multiplied by the absorption surface of a neutral. For our study, we have set $H = 2x_0$ and $\sigma_v n_{n,surf} = 5x_0^{-1}$, which corresponds to scale height of a typical neutral atmosphere, with respect to the size of our planetary obstacle. The ionosphere profile extends up to two planetary radius. The parameter changed among the various runs presented in this study is the total production rate Q which expression is:

$$Q = \int_V q_v dV \tag{2}$$

The aim of this study is to investigate topological variations between different ionospheric productions used as input in the ionospheric modeling. Our study is centered on super-Alfvénic type of interaction. The upstream plasma velocity chosen is 8 Alfvén Mach, which is typical at Earth, Venus and Mars. The plasma beta of the upstream plasma is $\beta e = 0.5$ and $\beta_i = 0.5$ at initialization, which is typical for solar wind condition. The ions inserted in the ionospheric model are set at $\beta = 0$ for ions and electrons, which corresponds to typical ionospheric ions at rest.

The parameters used in the run of the simulations presented in this paper are given in Table 2. We vary the production rate from 10 to 50 $10^3$ $Q_0$, where $Q_0$ is the normalized production rate, detailed in Table 1. We carry on our study on two species. We generate an ionosphere of pure ionized hydrogen ($H^+$) and an ionosphere of pure ionized oxygen ($O^+$). To illustrate the range of production rates from Table 2, one can compare them to Solar System obstacles' production rates. At Venus, a typical production rate is (Martinecz et al., 2009): $Q = 1.04 \times 10^{26}$ $s^{-1}$, which with $B_0 = 5$ nT and $n_0 = 5$ $cm^{-3}$ gives Q = 36,300 $Q_0$ (normalized following Table 1). Other values at Venus are given by Jarvinen et al. (2010), which provides another set of parameters: $B_0 = 10$ nT, $n_0 = 14$ $cm^{-3}$, $Q = 4.09 \times 10^{24}$ $s^{-1}$ for the production of $O^+$, and $Q = 6.42 \times 10^{24}$ $s^{-1}$ for $H^+$. This corresponds in our table of parameters to Q = 1200 $Q_0$ and Q = 1880 $Q_0$, for $H^+$ and $O^+$, respectively. At Mars, an example of the ionospheric production is furnished by Boesswetter et al. (2004), with $B_0 = 3$ nT, $n_0 = 4$ $cm^{-3}$, $Q = 5.37 \times 10^{25}$ $s^{-1}$ for a production of $O^+$. Once normalized according to Table 1, it corresponds to Q = 28,000 $Q_0$. Those values are specific production rates at a specific time. It is expected to observe a wide range of production values for those planets, depending on e.g. the solar cycles (Bougher et al., 1999), or seasonal variations (Yamauchi et al., 2015). The total ionization frequency of planetary ionospheres has to take into account the various mechanism occurring in it and remains a challenge (Lillis et al., 2015). In our model, we simplify as much as possible the interaction mechanisms occurring. Thus, we only use a total production factor Q, while the ion loss mechanism is performed by absorption at the surface of the obstacle, and particle escape at the simulation domain boundaries. The simulated ionospheres are produced using the total production rate Q. The production rate density at each point of the profile $q_v(r, \theta)$ (used later in the text) can easily be recovered from the total production rate. This is done by writing Eq. (1) in separate form. We define:

$$A_0 = \quad \kappa_v \sigma_v n_{n,surf} I_\infty \tag{3}$$

and

$$f(r, \theta) = exp\left(-\frac{r}{H} - \frac{\sigma_v n_{n,surf} H}{\cos\theta} \exp\left(-\frac{r}{H}\right)\right) \tag{4}$$

Thus, we write $q_v = A_0 f(r,\theta)$. Integrating over the half-shell where the ionosphere is generated, i.e. $r \in [R_p; 2R_p]$ and $\theta \in [0; \pi/2]$, where $\theta$ is the angle between the subsolar point and the terminator, yields:

$$Q = \int_{R_p}^{2R_p} \int_0^{\pi/2} \int_0^{2\pi} A_0 f(r, \theta) r^2 \sin\theta dr d\theta d\varphi = A_0 V_{char} \tag{5}$$

where we define the characteristic volume:

$$V_{char} = \int_{R_p}^{2R_p} \int_0^{\pi/2} \int_0^{2\pi} f(r, \theta) r^2 \sin\theta dr d\theta d\varphi \tag{6}$$

The characteristic volume is evaluated using parameters introduced earlier, i.e. $H = 2x_0$ and $\sigma_v n_{n,surf} = 5x_0^{-1}$:

$$V_{char} = 453 x_0^3 \tag{7}$$

The production density is retrieved from the expression:

$$q_v(r, \quad \theta) = \frac{Q}{V_{char}} f(r, \theta) \tag{8}$$

### 2.3. Currents

Describing currents in interplanetary plasma physics is an efficient manner to attach a deformation of the field to its corresponding physical process (Mauk and Zanetti, 1987), although one must keep in mind that the current is merely an indicator of the deformation of the field (Parker, 1996). The identification of the current system is made using simulation results. The details of each simulation are provided in the Supplementary material. In the core of the text, we will focus on describing the current system inferred from the simulation results and discuss their topologies. As we focus on unmagnetized, but ionosphere-rich obstacles, currents related to induced magnetosphere and unmagnetized obstacles are expected. Currents triggered by the interaction of the solar wind with an obstacle possessing an intrinsic field such as the Chapman-Ferraro currents, the Birkeland currents, the ring current, or storm related currents are not expected to be observed and will not be discussed in this paper. As we aim at providing a topological description of the interaction, we provide a short description of the topological currents encountered in our study:

(1) The telluric current. This current is attached to the conductivity of the planet and noted $j_{tel}$. It directly depends on the intrinsic conductivity of the planetary obstacle. Since we input in our model a finite conductivity to the obstacle, we expect to observe this current when no other current erases it.
(2) The pickup current. In the simulation results presented in this study, no collision is taken into account. Therefore, the only ion source comes from the production of ions in the ionosphere. Although they are produced with a zero velocity, they affect the total momentum. It appears that the effect of the produced ions can be expressed in the same manner as the collisional term, thus, the same expression as the Pedersen conductivity tensor can be used to

**Table 2**
List of the parameters used in the simulations presented in this paper. First column gives case name. Second column provides the normalized total production rate Q (see Eq. (2) and Table 1). The third column gives an overall estimation of the normalized dayside density at stationary state (see Auxiliary material). For every simulation, the upstream stellar wind is $u_{sw} = 8$ $v_{A,0}$, and the ionospheric ion beta is zero at initialization (see text).

| Case | Q[$Q_0$] | $n_{iono}$ [$n_0$] | Figure |
|---|---|---|---|
| $H^+$ | | | |
| 100$Q_0$\| $H^+$ | 100 | 0.01 | Fig. 1 |
| 10E3$Q_0$\| $H^+$ | $10.10^3$ | 1 | Fig. 2 |
| 50E3$Q_0$\| $H^+$ | $50.10^3$ | 10 | Fig. 3 |
| $O^+$ | | | |
| 250$Q_0$\| $H^+$ | 250 | 0.05 | Fig. 5 |
| 1E3$Q_0$\| $H^+$ | $1.10^3$ | 10 | Fig. 6 |
| 50E3$Q_0$\| $H^+$ | $50.10^3$ | 200 | Fig. 7 |

express an analogous conductivity for the production rate (see Neubauer (1998)). Injecting the production rate as a collision frequency in the Pedersen conductivity gives:

$$\sigma(r,\theta)=\frac{q_v/n}{(q_v/n)^2+\Omega_i^2}\frac{nq_i^2}{m_i} \quad (9)$$

where the terms $\Omega_i$, $q_i$, and $m_i$ are the ion gyro frequency, charge, and mass. Later in the text, we present results of the conductivity of the ionosphere using this reasoning. Even if we describe the interaction using the pickup current, the deformation of the field, propagating at the Alfvén velocity, generates the current (Vasyliunas, 2006). It is important to note that the current linked to the magnetopause, in the simulation results presented in this study, is induced by the pickup current, and both currents merge on the dayside. This makes it hard to distinguish topologically between those two currents in this region. The induced magnetopause and the pickup current are parallel in the dayside (along the direction of the electric field). Discriminating between the currents of the compressed induced field (magnetopause) and the pickup current would require a simulation with a significantly higher resolution, and a dedicated study. This falls out of the scope of this study.

(3) The magnetotail currents. Typical magnetotail currents in induced magnetosphere have been studied in the literature using measurements at Mars and Venus (Rong et al., 2015). It exhibits a typical theta-like configuration for fully developed interaction types. Even if the nightside region is populated with ionospheric ions triggering local currents, a global current directed along the convective electric field flows in the equatorial plane. It is clear that the magnetotail is a place of various dynamic mechanisms. However, in our simulations the steady conditions of the inflow – even using constant addition of ionospheric ions – result in a steady magnetotail.

## 3. Results

We introduce the results from our simulations using three-dimensional schematics. The first half of this section is dedicated to the description of the currents and the interaction region topology for various production rates of a pristine $H^+$ ionosphere. The second half describes the currents system of the interaction region for a pristine $O^+$ ionosphere and several production rates.

### 3.1. Low to high production rates for an $H^+$ ionosphere

The first type of topological interaction, which is encountered when increasing the production rate in our simulation, is the $100Q_0|H^+$ case, shown in Fig. 1. We recall that the upstream plasma flows along $+x$ and the IMF is along $-z$. The production rate used in that simulation is $Q=100\ Q_0$. Such a production rate results in a dayside density of $n_{iono}=0.01\ n_0$ at steady state. Details of the parameters are provided in Table 2. As we populate the ionosphere, a pronounced asymmetry rises up between the dawn side and the dusk side of the interaction region. Such an asymmetry already exists for unmagnetized ionosphere-less obstacles, mostly in the nightside region of the interaction region due to the gyromotion of the ions (Umeda, 2012). In the simulation diagram of Fig. 1, the asymmetry becomes noticeable in the total density and magnetic field (see Figs. S1b and S1d). A weak polarization current $j_{fast}$ (drawn with square blue arrows) is observable in the equatorial plane, superimposed to the telluric current $j_{tel}$ (yellow arrow) on the dayside of the obstacle. We identify the polarization current by deriving it from the formula and comparing it to the general total current. In this regime, no clear ionopause is yet defined, as the IMF fully penetrates the ionosphere. The pressure of the induced field on the dayside is not sufficient to balance the inflowing plasma. In the nightside of the interaction region, the wake of the obstacle is bounded by a typical

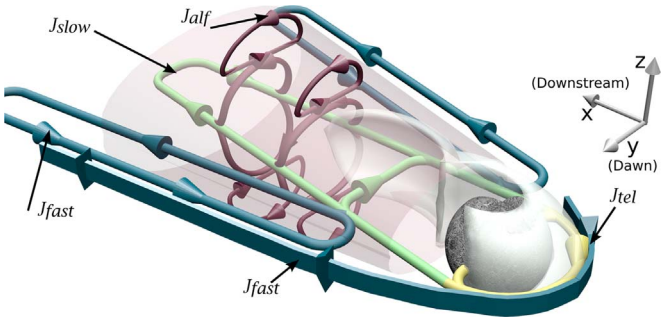


**Fig. 1.** Three-dimensional diagram of the $100Q_0|\ H^+$ system (see parameters in Tables 2). The IMF is along $-z$, the stellar wind flows along $+x$, and the obstacle radius is $20x_0$. The trajectory of the ionospheric ions is represented by a semi-transparent white trail. The slow mode diamagnetic ($j_{slow}$), telluric ($j_{tel}$), fast mode polarization ($j_{fast}$), Alfvénic ($j_{alf}$), bow-shock ($j_{bs}$), currents are colored in green, yellow, blue, red, purple, red, respectively. (For interpretation of the references to color in this figure, the reader is referred to the web version of this article.)

diamagnetic current related to the propagation of slow magnetosonic waves, extensively described in the literature (Roussos et al., 2008). Because this type of interaction is quite similar to that of an ionosphere-less obstacle (such as the Moon), a fast magnetosonic mode polarization current $j_{fast}$ (represented in blue) is present in the nightside of the interaction region, on the outer dawn and dusk parts. It should be noted that the dayside asymmetry induced by the implemented ionosphere moves the dawn part of the fast-related mode current tailward, compared to its dusk part. The northern and southern parts of the tail present an Alfvénic current (plotted in red in the diagram). The presence of Alfvénic currents in the nightside of the interaction region here has similar origin to that of an unmagnetized, airless obstacle, which has been discussed earlier (Simon et al., 2012; Vernisse et al., 2013).

Fig. 2 displays a diagram of simulation results for the $10E3Q_0|\ H^+$. The obstacle possesses an ionosphere with a production rate of $Q=10\ 10^3\ Q_0$. In this type of interaction, the ionosphere is as dense as the upstream plasma with $n_{iono}=1\ n_0$. The mass loading is sufficient to decelerate significantly the impinging plasma. A bow-shock is visible in this interaction type, noticeable by the increase in temperature (see Supplementary material), articulated around the bow-shock current (purple arrows - $j_{bs}$). Behind the bow-shock region, the magnetic field piles up, and two boundaries are noticeable (Zhang et al., 1991, Russell et al., 2006). The external one is the magnetic boundary, or the induced magnetopause. In this case, the magnetic field reaches about two times the background magnetic field (see Figs. S2a and S2b). The internal boundary is the ionopause. It separates the region dominated by the ionospheric plasma from the interplanetary medium. The magnetic field diminishes in that region (see Figs. S2a and S2k). The pick-up current $j_{pck}$ is present between the ionopause and the induced magne-

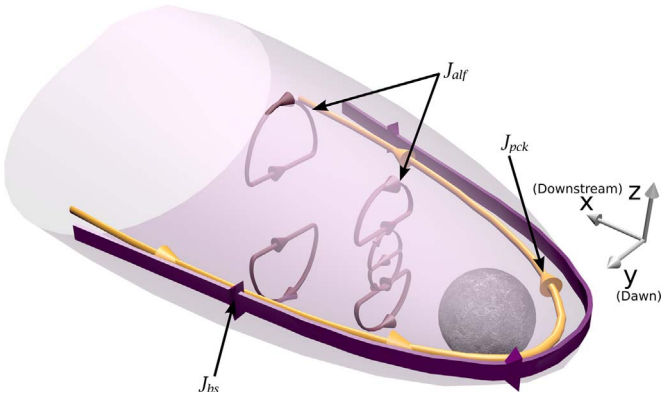


**Fig. 2.** Same as Fig. 1 for the $10E3Q_0|\ H^+$ case. (For interpretation of the references to color in this figure, the reader is referred to the web version of this article.)

topause. It flows from the dawn side of the interaction region to the dusk side. This current is generated by the acceleration of the ionospheric ions, which get picked-up. We identify this current by evaluating it in the region of the Chapman ionosphere. The details are provided in the Supplementary material. Because the ionosphere we study is constituted of $H^+$ ions, and their gyroradius is comparable to the obstacle radius in this simulation, the resulting asymmetry does not significantly alter the dayside topology. The interaction region remains symmetric. The nightside of the interaction is populated with ionospheric ions and the typical wake slow mode related diamagnetic current has vanished, as well as the fast mode current. The current in the nightside is structured in the equatorial plane by the motion of the ionospheric ions. The closest part (under $100x_0$) of the nightside region is constituted of two loops of currents. The inner current (closest to the equatorial plane) flows clockwise in the northern lobe and anti-clockwise in the southern lobe for an observer looking at the tail and sitting on the north pole of the obstacle. The external current loops flows in opposite direction – anticlockwise at the northern lobe and clockwise at the southern lobe. The distant tail is structured around two loops of current, flowing in the convective electric field direction in its inner part, reaching the external part via field aligned currents, and closing by the bow-shock current. We use the denomination Alfvénic current $j_{alf}$ as it is linked to the deformation of the field along the axis of propagation, and no particular modification of the density and the magnetic field magnitude are observed in the middle of each lobe (see Fig. S2).

Fig. 3 provides a schematic overview of the $50E3Q_0|\ H^+$ case. The production rate used in that simulation is $Q = 50\ 10^3\ Q_0$. Such interaction is close to a Venus-like type of interaction. A bow shock is well defined, as well as the induced magnetopause and ionopause. The dayside density of the ionosphere behind the ionopause reaches about $n_{iono} = 10\ n_0$ in average, in steady state. The interaction region is symmetric between the dawnside and the duskside regions. The global interaction region is structured around few currents. On the dayside, the bow-shock current $j_{bs}$ flows from dusk to dawn (purple arrows). The shape of the bow-shock in the interaction region is represented by the purple semi-transparent layer. Even in this regime of interaction, the induced magnetopause is hardly distinguishable from the bow shock (see Fig. S3k). Since the induced magnetopause current and the bow-shock are expected to flow in the same direction, we do not draw any distinct currents. The pickup current $j_{pck}$ (plotted in orange), flows from dawn to dusk and follows the main circuit of the ionospheric ion. The magnetotail current (displayed in red) is consistent with the field line draping around the interaction region, and the formation of northern and southern lobes. It flows from dusk to dawn on the southern and northern limit, and flows from dawn to dusk in the equatorial plane – anti-clockwise for the northern lobe and clockwise for the southern lobe. The magnetotail current merely structures the nightside of the

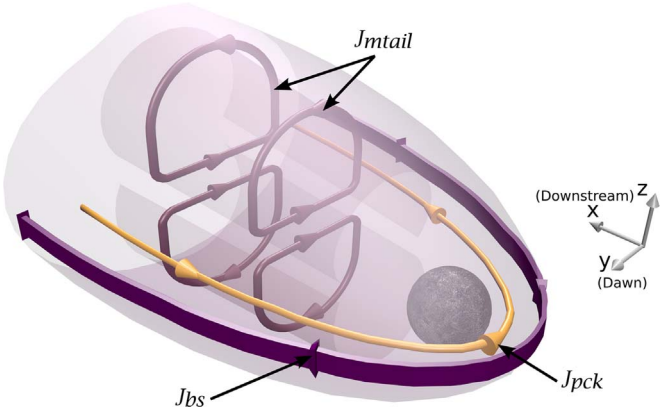


**Fig. 3.** Same as Fig. 1 for the $50E3Q_0|\ H^+$ case. (For interpretation of the references to color in this figure, the reader is referred to the web version of this article.)

interaction region. It results from the global draping of the IMF lines. As we limit ourselves to major currents, we do not provide the detail of the many currents appearing in the tail. Owing to the population of the tail by ionospheric ions, variations in densities and temperatures may appear and create field distortions and associated currents. Those currents may be identifiable using dedicated magnetotail simulation runs with much higher grid resolution in that region.

Fig. 4a represents the pickup conductivity derived using the production factor in the Pedersen tensor (see Eq. (7) and Neubauer, 1998). The conductivity is calculated based on the density provided by the simulation results. Fig. 4b displays a similar profile using the magnetic Reynolds number detailed in the appendix. The different curves show the results for production rates of $Q = 100$, $10^3$, $10^4$, 25 $10^3$, and 50 $10^3$ $Q_0$. Considering the ionosphere as a highly conducting shell, one can derive the current and magnetic field resulting from the induction due to the convection of the IMF. We approximate the magnetic pressure and calculate the pressure balance (between the induced magnetic field pressure and the solar wind dynamic pressure) using the production rate on one side and the upstream plasma ram pressure on the other side. This calculation is detailed in the appendix. In our case, the ionosphere is capable of generating a sufficient induced magnetic field that is able to balance the stellar wind ram pressure if its Reynolds number is above 8 (see Eq. (A1)). This is represented by a black line at $R_e = 8$ in Fig. 4b. Such a condition is fulfilled when the production rate reaches about $Q = 1000\ Q_0$ for a purely $H^+$ ionosphere. Such a production rate results at steady state in our simulations in a dayside density about $n = 0.1\ n_0$.

### 3.2. Low to high production rates for an $O^+$ generated ionosphere

In this section, the simulated ionosphere has been generated using only heavy ions ($O^+$) to emphasize the role of the ionospheric ion mass. The first regime of interaction is displayed in Fig. 5. It shows a noticeable influence from the ionospheric ions, and corresponds to the $250Q_0|\ O^+$ case. The production rate is $Q = 250\ Q_0$. The average density of the ionosphere when the simulation has reached steady state is about $n_{iono} = 0.05\ n_0$. In this regime, the interaction region becomes asymmetric. Due to oxygen picked up at the dayside, the impinging solar wind is slowed down on the gyration path of the oxygen ions. The density of oxygen ions is sufficient to drape significantly the inflowing magnetic field. The draping of the field line is evinced by the pickup current $j_{pck}$ represented in orange. However, the draping is not sufficient to create a distinct pile up of the magnetic field in the region populated with planetary ions at rest or accelerated (See Fig. S4b). The current related to the bow-shock – or fast magnetosonic waves compressed on the dayside – is faint but observable. It is represented in purple, with the distribution depicted by the purple semi-transparent layer. Evidences of this current are detailed in the Supplementary material. In particular, an increase in temperature is visible, although it is not clear if the fast wave has reached its non-linear stage. While the dusk side of the interaction region is highly asymmetric owing to the pick-up and the direction of the IMF, the dawn side of the interaction region remains close to the $H^+$ ionosphere depicted earlier. The nightside region presents a typical lunar-type interaction void bounded by slow mode diamagnetic current $j_{slow}$ and fast mode polarization current $j_{fast}$ (Fatemi et al., 2013; Vernisse et al., 2013). The latter current shows however an asymmetric pattern owing to the larger gyroradius of $O^+$.

The simulation regime $1E3Q_0|\ O^+$ with an ionospheric production of $Q = 1 \times 10^3\ Q_0$ using a pristine $O^+$ rich ionosphere is depicted in Fig. 6 using the currents structures. The interaction region is delimited by a clear bow-shock and the induced magnetosphere is clearly developed on the dayside and the nightside (see Fig. S5a-d where the magnetic field and density jumps with values of several times the upstream plasma are identifiable). The density of the ionosphere on the dayside is close to $n_{iono} = 10\ n_0$. The dayside interaction region is

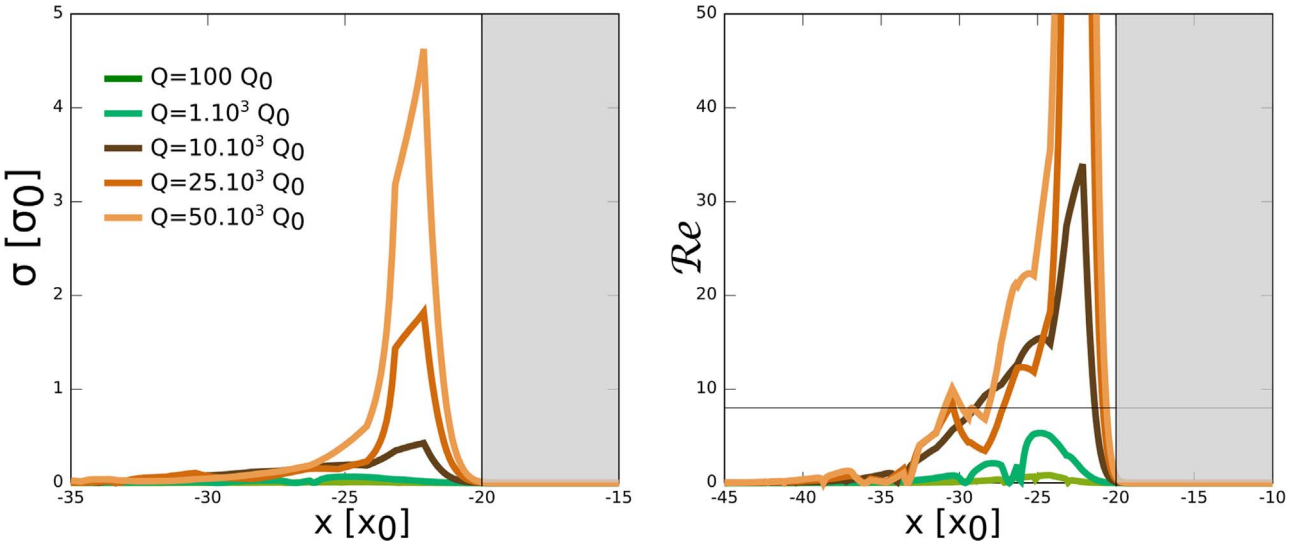


**Fig. 4.** (a) Pickup (or equivalent Pedersen) conductivity and (b) Reynolds magnetic number along the x-axis. The pickup conductivity is expressed in normalized units (see Table 1). The expression is given by Eq. (7). The magnetic Reynolds is used to show the pressure equilibrium condition at $R_e = 8$ (see Appendix). The obstacle is represented by the gray shadowed region. The simulation geometry and parameters are provided in Section 2. (For interpretation of the references to color in this figure, the reader is referred to the web version of this article.)

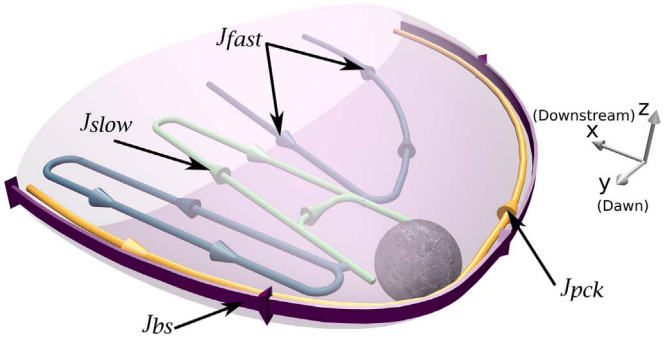


**Fig. 5.** Same as Fig. 1 for the $250Q_0|\ H^+$ case.

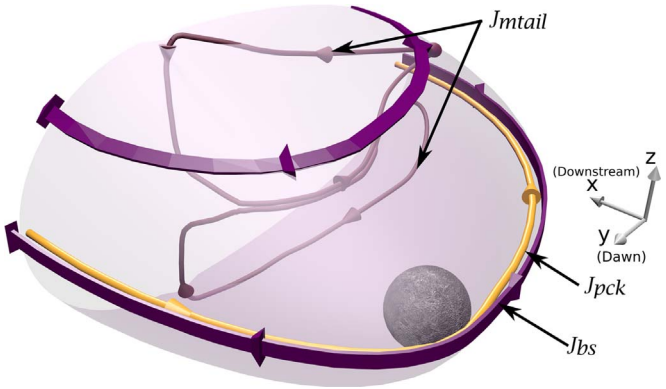


**Fig. 6.** Same as Fig. 1 for the $1E3Q_0|\ H^+$ case. (For interpretation of the references to color in this figure, the reader is referred to the web version of this article.)

delimited by a fully developed bow shock depicted by the purple semi-transparent layer and related to its current $j_{bs}$ in purple. The ionospheric ions picked up trigger a current $j_{pck}$ depicted in orange and flowing from dawn to dusk. The nightside of the interaction region is structured around a strongly asymmetric magnetotail (associated with the current $j_{mtail}$). This current flows in the direction of the electric field in the equatorial plane (along $-y$). It follows the shape of the induced magnetosphere on its dusk side. The magnetotail current merges with the pickup current in the equatorial duskside region. It is closed by the bow-shock current in the north and south boundaries. No significant

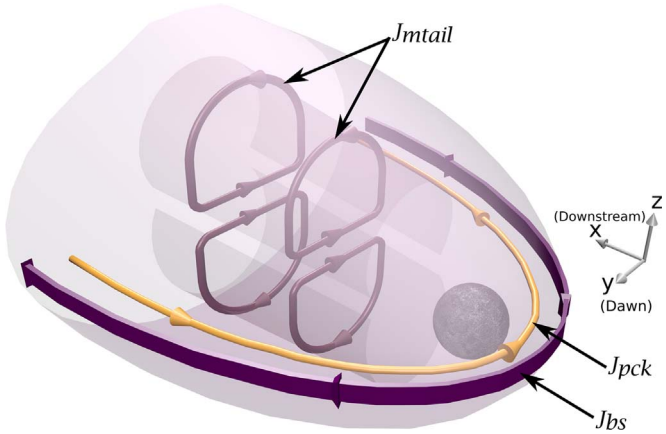


**Fig. 7.** Same as Fig. 1 for the $50E3Q_0|\ H^+$ case. (For interpretation of the references to color in this figure, the reader is referred to the web version of this article.)

current is identifiable on the dawn side of the interaction region, between the bow shock and the magnetotail current.

Fig. 7 depicts the currents in the interaction region for the $50E3Q_0|\ O^+$ regime of interaction, using an ionospheric production rate of $Q = 50\ 10^3\ Q_0$. The mean density at the dayside of the obstacle far exceeds the upstream plasma density, with $n_{iono} = 200\ n_0$. Consequently, the mass loading of the impinging magnetic field is similar to a highly conducting shell encompassing the planetary obstacle. The first noticeable aspect is that the interaction region becomes more symmetric. As the ionospheric ion production is increased, the gyro motion of the ionospheric ions is contained in the center of the tail. This effect is simply due to the increase of magnetic field magnitude at the pile up region, directly generated by the increase of the production rate. Increasing the magnetic field decreases the gyroradius of the picked up ionospheric particles, and thus the asymmetry. This effect brings the topological changes of a pristine $O^+$ generated ionosphere closer to a type of interaction using a pristine $H^+$ ionosphere. The main currents that can be identified in this interaction regime are the bow shock current $j_{bs}$ and the pickup current $j_{pck}$, merged with the induced magnetopause current on the dayside, represented in purple an orange, respectively. The pick-up current flows from dawn to dusk, following the path of the ionospheric ions, related to the orientation of the IMF ($-z$ – or southward – in our case). The

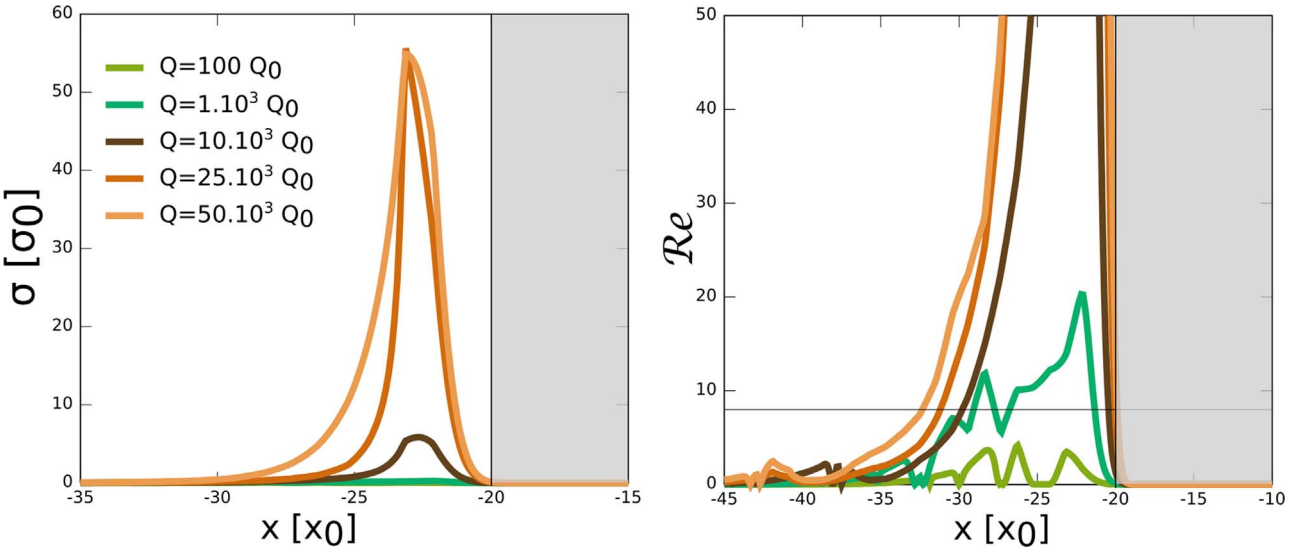


**Fig. 8.** Same as Fig. 4 for the $O^+$ cases. (For interpretation of the references to color in this figure, the reader is referred to the web version of this article.)

nightside of the interaction region is structured by two major lobes bounded by a magnetotail current forming a typical theta-like pattern. The northern magnetotail current flows anti-clockwise for an observer sitting at the north pole of the obstacle, while the southern magnetotail current flows clockwise, seen by the same observer (red currents $j_{mtail}$).

The pickup conductivity (Eq. (7)) along with the magnetic Reynolds number – detailed in the appendix – are plotted along the subsolar line of sight (x, y = 0, z = 0) in Fig. 8. Similarly to Fig. 4, the condition for an ionosphere to be sufficiently dense to trigger a bow shock is represented by the black line in Fig. 8b with $R_e = 8$ (see Appendix for details). Five interaction regimes are represented, with $Q = 100$, $1\times10^3$, $10\times10^3$, $25\times10^3$, and $50\times10^3$ $Q_0$. With a pristine $O^+$ ionosphere rich obstacle, the condition to trigger a bow shock is already fulfilled for $Q = 1\ 10^3\ Q_0$. In addition, the conductivity reaches a limit after $Q = 25\times10^3\ Q_0$. This result suggests the tendency that an ionosphere, even having a high production rate, will reach a limit in the magnetic field that it induces. Therefore, after a maximum conductivity is reached, the only possibility to extent further the magnetospheric cavity is to change other ionospheric parameters, as the scale height of the atmosphere, which in case of an extended ionosphere far away from the obstacle, would lead to an increase of the size of the interaction region.

## 4. Discussion

The various interaction types presented in the previous section are summarized using the structure of the currents flowing in the interaction region. In this section, we discuss the evolution of the topology and the currents. We divide the currents in three main groups, representing the stages of interaction, when they are noticeable. Each stage is identified by a particular production rate, depending on the ionospheric species. Ionospheric induced effects appear at lower production rate for $O^+$ ionospheric ions than for $H^+$.

### 4.1. Weak ionosphere and lunar-type currents

Prior to the apparition of any effect due to the ionospheric ions, the interaction region is similar to that of a lunar type obstacle, already well described in the literature (e.g. Gharaee et al., 2015). The current system in a lunar type regime is limited to the nightside of the interaction region, and constituted of Alfvénic, fast and slow magnetosonic currents. The first feature that appears is situated at the dawn side terminator. This signature is attached to a current flowing from dusk to dawn, limited to the equatorial plane, and which becomes the bow-shock current at higher production rates (Figure 1). In the case of a preexisting telluric current as it is the case in our simulation, the fainted bow-shock current increases the total magnitude of the currents in that region. The secondary asymmetry comes from the pickup effect and the population of the dusk side of the interaction region with planetary ions. However the effect of the pickup ions in the dusk side region becomes noticeable only at higher production rates (after $Q = 1\times10^3$ $Q_0$ for $H^+$ ions and $Q = 250$ $Q_0$ for $O^+$ ions).

### 4.2. Intermediate ionosphere: the role of the pickup current

In the intermediate interaction regimes, the pickup current becomes significant and drives a strong asymmetry, particularly in the dusk side of the interaction region. The transfer of momentum between the upstream plasma and the picked-up ionospheric ions happens not only at the dayside of the obstacle, but also along the gyro path of the picked-up particles (see e.g. Fig. S5j). This effect is particularly noticeable for the pristine $O^+$ ionosphere, owing to the size of the obstacle ($20x_0$) in comparison to the gyroradius ($8x_0$ for $H^+$ and $128x_0$ for $O^+$ at 8 Alfvén Mach). In this regime of interaction, the induced magnetic field is significant with $B = 2\ B_0$ in front of the ionopause, but likely not sufficient to fully balance the solar wind pressure on its own. The conductivity and the condition for sustaining the upstream plasma pressure are provided in Figs. 4 and 8. However, once the condition is achieved, the plasma is slowed down. In this regime of interaction, the nightside region becomes populated with ionospheric ions in the case of the $H^+$ ionosphere. Although with $O^+$ the nightside of the interaction region is not populated with ionospheric ions owing to their larger gyroradii, the nightside region is strongly influenced by the dayside draping, resulting in a main electric field directed current in the nightside equatorial plane. This type of interaction has not been observed yet and may be not present in the Solar system. The main reason may be that in this regime, the ionosphere is not sufficiently shielded from the impinging plasma, and the atmosphere will be constantly eroded until being fully taken away.

### 4.3. Strong ionosphere: bow-shock and induced magnetopause and magnetotail currents

The last regime is the fully developed interaction with the typical bow-shock, magnetopause and magnetotail. As noticed earlier, in this type of regime, the interaction region becomes symmetric, either with the $H^+$ ionosphere (which was already quite symmetric owing to the limited gyroradius) or with the $O^+$ ionosphere. Differences between the two types of ionosphere remain in the global size of the whole

interaction region, larger for about 10% for the $O^+$ case (see Figs. S3 and S6). In this interaction regime, the mass loading is sufficient to build up a magnetic field sustaining the upstream plasma pressure (Lundin, 2011). This corresponds to the typical cases of the Mars and Venus interaction type. Although the global topology of this interaction regime is easily described by a simple global draping of the magnetic field around the planet, the structures that may be driven by the ionospheric ions in the nightside region are numerous, and their systematic study falls out of the scope of this study.

## 5. Conclusions

Interactions of a super-Alfvénic stellar wind with obstacles possessing an ionosphere are diverse in the Solar system, and possibly in extra-solar systems. Either for tenuous or dense ionospheres, planetary particles in such types of interactions are expected to trigger specific effects. We summarize the global topology of our simulations results into three-dimensional diagrams. Our study shows that noticeable effects arise when the ionospheric density on the dayside of the obstacle is on average ten times under the upstream plasma density. However, heavier ionospheric ions will slow down more efficiently the impinging solar wind, thus requiring a lower dayside density to introduce noticeable effects. Weakly dense ionospheres (ten times under the upstream plasma density) introduce a perturbation of the general interaction region – at the beginning close to a lunar type case – seen in the magnetic field asymmetry on the dawn side of the region at first. At higher densities (about five times under the background density), pickup ions induce a moderate pile up on the dusk side of the interaction region, behind the terminator plane, along the trajectory of the picked up particles. At stronger ionospheric densities – or production rate – the magnetic pile-up at the dayside of the obstacle increases and a fully developed induced magnetosphere and a bow-shock appear. The nightside region in this regime is driven by the dayside pile up, as the bending of the IMF due to the mass loading create a typical magnetotail-like structure. Eventually, the shape of the magnetopause cavity becomes more symmetric as the dayside production rate increases, but remains broader for heavier ions compared to lighter ionospheric ions.

## Acknowledgements

Yoann Vernisse acknowledged a Post-Doctoral fellowship at the International Max Planck Research School on Physical Processes in the Solar System and beyond.

Jerermy Riousset's work has been supported by grant CRC 963.

The simulations were performed on the systems of the North-German Supercomputing Alliance.

## Appendix A. Reynolds number

A condition providing the necessary conductivity to sustain the upstream pressure can be evaluated using several assumptions. Considering the induced field generated by the pickup current, we can write:

$$j_{pck}=\sigma E_{IMF}=\sigma\,(u_{sw}\times B_{IMF})\,B_{induced}=\mu_0 j_{pck}\,L_{char}=\mu_0 L_{char}\,\sigma\,(u_{sw}\times B_{IMF}) \tag{A1}$$

where $L_{char}$ is the characteristic length of the system, resulting from the ratio between the surface of integration of the magnetic field and the length of integration of the current. If we assume that the length $L_{char}$ represents also the distance over which the field is convected (which is close in this case), we get:

$$B_{induced}=R_e B_{IMF} \tag{A2}$$

Assuming that only the induced field sustains the solar wind dynamic pressure, one can write:

$$\frac{1}{2}\rho u_{sw}^2\leq\frac{B_{induced}^2}{2\mu_0}\quad\Leftrightarrow\quad u_{sw}^2\leq R_e^2 v_{A,0}^2\quad\Rightarrow\quad\frac{u_{sw}}{v_{A,0}}\leq R_e \tag{A3}$$

Thus, the induced field is able to sustain an upstream plasma flowing at Alfvén Mach number 8 if the Reynolds number is above 8.

## Appendix B. Supporting information

Supplementary data associated with this article can be found in the online version at doi:10.1016/j.pss.2017.01.012.

## References

Bagdonat, T., Motschmann, U., 2002a. From a weak to a strong comet − 3D global hybrid simulation studies. Earth Moon Planets 90, 305–321. http://dx.doi.org/10.1023/A:1021578232282.

Bagdonat, T., Motschmann, U., 2002b. 3D hybrid simulation code using curvilinear coordinates. J. Comput. Phys. 183, 470–485. http://dx.doi.org/10.1006/jcph.2002.7203.

Bauer, S.J., Brace, L.H., Hunten, D.M., Intriligator, D.S., Knudsen, W.C., Nagy, A.F., Russell, C.T., Scarf, F.L., Wolfe, J.H., 1977. The Venus ionosphere and solar wind interaction. Space Sci. Rev. 20, 413–430. http://dx.doi.org/10.1007/BF02186461.

Baumjohann, W., Blanc, M., Fedorov, A., Glassmeier, K.-H., 2010. Current systems in planetary magnetospheres and ionospheres. Space Sci. Rev. 152, 99–134. http://dx.doi.org/10.1007/s11214-010-9629-z.

Baumjohann, W., Treumann, R.A., 1996. Basic Space Plasma Physics. Imperial College Press, London, UK.

Biver, N., Bockelée-Morvan, D., Colom, P., Crovisier, J., Germain, B., Lellouch, E., Davies, J.K., et al., 1997. Long-term evolution of the outgassing of Comet Hale-Bopp from radio observations. Earth Moon Planets 78, 5–11. http://dx.doi.org/10.1023/A:1006229818484.

Boesswetter, A., Bagdonat, T., Motschmann, U., Sauer, K., 2004. Plasma boundaries at Mars: a 3-D simulation study. Ann. Geophys. 22, 4363–4379. http://dx.doi.org/10.5194/angeo-22-4363-2004.

Bougher, S.W., Engel, S., Roble, R.G., Foster, B., 1999. Comparative terrestrial planet thermospheres 2. Solar cycle variation of global structure and winds at Equinox. J. Geophys. Res. 104, 16591–16611. http://dx.doi.org/10.1029/1998JE001019.

Cravens, T.E., 1987. Theory and observations of cometary ionospheres. Adv. Space Res. 7, 147–158. http://dx.doi.org/10.1016/0273-1177(87)90212-2.

Curry, S.M., Luhmann, J., Ma, Y., Liemohn, M., Dong, C., Hara, T., 2015. Comparative pick-up ion distributions at Mars and Venus: consequences for atmospheric deposition and escape. Planet. Space Sci. 115, 35–47. http://dx.doi.org/10.1016/j.pss.2015.03.026.

Davis, S., Marshall, J., Richard, D., Adler, D., Adler, B., 2014. Scattering properties of lunar dust analogs. Planet. Space Sci. 90, 28–36. http://dx.doi.org/10.1016/j.pss.2013.11.005.

Fatemi, S., Holmström, M., Futaana, Y., Barabash, S., Lue, C., 2013. The lunar wake current systems. Geophys. Res. Lett. 40, 17–21. http://dx.doi.org/10.1029/2012GL054635.

Fatemi, S., Holmström, M., Futaana, Y., Lue, C., Collier, M.R., Barabash, S., Stenberg, G., 2014. Effects of protons reflected by lunar crustal magnetic fields on the global lunar plasma environment. J. Geophys. Res. (Space Phys.) 119, 6095–6105. http://dx.doi.org/10.1002/2014JA019900.

Gharaee, H., Rankin, R., Marchand, R., Paral, J., 2015. Properties of the lunar wake predicted by analytic models and hybrid-kinetic simulations. J. Geophys. Res. (Space Phys.) 120, 3795–3803. http://dx.doi.org/10.1002/2014JA020907.

Jarvinen, R., Brain, D.A., Luhmann, J.G., 2016. Dynamics of planetary ions in the induced magnetospheres of Venus and Mars. Planet. Space Sci. 127, 1–14. http://dx.doi.org/

10.1016/j.pss.2015.08.012.
Jarvinen, R., Kallio, E., Dyadechkin, S., Janhunen, P., Sillanpää, I., 2010. Widely different characteristics of oxygen and hydrogen ion escape from Venus. Geophys. Res. Lett. 37, 16201. http://dx.doi.org/10.1029/2010GL044062.
Jarvinen, R., Kallio, E., Janhunen, P., Barabash, S., Zhang, T.L., Pohjola, V., Sillanpää, I., 2009. Oxygen ion escape from Venus in a global hybrid simulation: role of the ionospheric $O^+$ ions. Ann. Geophys. 27, 4333–4348. http://dx.doi.org/10.5194/angeo-27-4333-2009.
Jia, X., Slavin, J.A., Gombosi, T.I., Daldorff, L.K.S., Toth, G., Holst, B., 2015. Global MHD simulations of Mercury's magnetosphere with coupled planetary interior: induction effect of the planetary conducting core on the global Interaction. J. Geophys. Res. (Space Phys.) 120, 4763–4775. http://dx.doi.org/10.1002/2015JA021143.
Johansson, E.P.G., Bagdonat, T., Motschmann, U., 2009. Consequences of expanding exoplanetary atmospheres for magnetospheres. Astron. Astrophys. 496, 869–877. http://dx.doi.org/10.1051/0004-6361/200810509.
Kriegel, H., Simon, S., Motschmann, U., Saur, J., Neubauer, F.M., Persoon, A.M., Dougherty, M.K., Gurnett, D.A., 2011. Influence of negatively charged plume grains on the structure of Enceladus' Alfvén Wings: hybrid simulations versus Cassini magnetometer data. J. Geophys. Res. 116 (A15), 10223. http://dx.doi.org/10.1029/2011JA016842.
Kriegel, H., Simon, S., Müller, J., Motschmann, U., Saur, J., Glassmeier, K.-H., Dougherty, M.K., 2009. The plasma interaction of Enceladus: 3D hybrid simulations and comparison with Cassini MAG data. Planet. Space Sci. 57, 2113–2122. http://dx.doi.org/10.1016/j.pss.2009.09.025.
Kulikov, Y.N., Lammer, H., Lichtenegger, H.I.M., Penz, T., Breuer, D., Spohn, T., Lundin, R., Biernat, H.K., 2007. A comparative study of the influence of the active young Sun on the early atmospheres of Earth, Venus, and Mars. Space Sci. Rev. 129, 207–243. http://dx.doi.org/10.1007/s11214-007-9192-4.
Lillis, R.J., Brain, D.A., Bougher, S.W., Leblanc, F., Luhmann, J.G., Jakosky, B.M., Modolo, R., et al., 2015. Characterizing atmospheric escape from Mars today and through time, with MAVEN. Space Sci. Rev. 195, 357–422. http://dx.doi.org/10.1007/s11214-015-0165-8.
Lipatov, A.S., Cooper, J.F., Sittler Jr., E.C., Hartle, R.E., 2012. Effects of $Na^+$ and $He^+$ pickup ions on the lunar-like plasma environment: 3D hybrid modeling. Adv. Space Res. 50, 1583–1591. http://dx.doi.org/10.1016/j.asr.2012.07.009.
Lundin, R., 2011. Ion acceleration and outflow from Mars and Venus: an overview. Space Sci. Rev. 162, 309–334. http://dx.doi.org/10.1007/s11214-011-9811-y.
Marchaudon, A., Blelly, P.-L., 2015. A new interhemispheric 16-moment model of the plasmasphere-ionosphere system: IPIM. J. Geophys. Res. (Space Phys.) 120, 5728–5745. http://dx.doi.org/10.1002/2015JA021193.
Martinecz, C., Boesswetter, A., Fränz, M., Roussos, E., Woch, J., Krupp, N., Dubinin, E., et al., 2009. Plasma environment of Venus: comparison of Venus Express ASPERA-4 measurements with 3-D hybrid simulations. J. Geophys. Res. 114, 0. http://dx.doi.org/10.1029/2008JE003174.
Mauk, B.H., Zanetti, L.J., 1987. Magnetospheric electric fields and currents. Rev. Geophys. 25, 541–554. http://dx.doi.org/10.1029/RG025i003p00541.
Motschmann, U., Kührt, E., 2006. Interaction of the solar wind with weak obstacles: hybrid simulations for weakly active comets and for Mars. Space Sci. Rev. 122, 197–208. http://dx.doi.org/10.1007/s11214-006-6218-2.
Mueller, J., Simon, S., Motschmann, U., Glassmeier, K.-H., Saur, J., Schüle, J., Pringle, G.J., 2010. Magnetic field fossilization and tail reconfiguration in Titan's plasma environment during a magnetopause passage: 3D adaptive hybrid code simulations. Planet. Space Sci. 58, 1526–1546. http://dx.doi.org/10.1016/j.pss.2010.07.018.
Mueller, J., Simon, S., Motschmann, U., Schüle, J., Glassmeier, K.-H., Pringle, G.J., 2011. A.I.K.E.F.: adaptive hybrid model for space plasma simulations. Comput. Phys. Commun. 182, 946–966. http://dx.doi.org/10.1016/j.cpc.2010.12.033.
Mueller, J., Simon, S., Wang, Y.-C., Motschmann, U., Heyner, D., Schüle, J., Ip, W.-H., Kleindienst, G., Pringle, G.J., 2012. Origin of Mercury's double magnetopause: 3D hybrid simulation study with A.I.K.E.F. Icarus 218, 666–687. http://dx.doi.org/10.1016/j.icarus.2011.12.028.
Neubauer, F.M., 1998. The Sub-Alfvénic interaction of the Galilean Satellites with the Jovian Magnetosphere. J. Geophys. Res. 103, 19843–19866. http://dx.doi.org/10.1029/97JE03370.
Parker, E.N., 1996. The alternative paradigm for magnetospheric physics. J. Geophys. Res. 101, 10587–10626. http://dx.doi.org/10.1029/95JA02866.
Phillips, J.L., Luhmann, J.G., Russell, C.T., Moore, K.R., 1987. Finite Larmor radius effect on ion pickup at Venus. J. Geophys. Res. 92, 9920–9930. http://dx.doi.org/10.1029/JA092iA09p09920.
Rong, Z.J., Barabash, S., Stenberg, G., Futaana, Y., Zhang, T.L., Wan, W.X., Wei, Y., Wang, X.D., Chai, L.H., Zhong, J., 2015. The flapping motion of the Venusian magnetotail: Venus express observations. J. Geophys. Res. (Space Phys.) 120, 5593–5602. http://dx.doi.org/10.1002/2015JA021317.
Roussos, E., Müller, J., Simon, S., Bö/s swetter, A., Motschmann, U., Krupp, N., Fränz, M., Woch, J., Khurana, K.K., Dougherty, M.K., 2008. Plasma and fields in the wake of Rhea: 3-D hybrid simulation and comparison with Cassini data. Ann. Geophys. 26, 619–637. http://dx.doi.org/10.5194/angeo-26-619-2008.
Russell, C.T., Luhmann, J.G., Strangeway, R.J., 2006. The solar wind interaction with Venus through the eyes of the Pioneer Venus Orbiter. Planet. Space Sci. 54, 1482–1495. http://dx.doi.org/10.1016/j.pss.2006.04.025.
Simon, S., 2015. An analytical model of Sub-Alfvénic Moon-Plasma interactions with application to the hemisphere coupling effect. J. Geophys. Res. (Space Phys.) 120, 7209–7227. http://dx.doi.org/10.1002/2015JA021529.
Simon, S., Boesswetter, A., Bagdonat, T., Motschmann, U., Glassmeier, K.-H., 2006. Plasma environment of Titan: a 3-D hybrid simulation study. Ann. Geophys. 24, 1113–1135. http://dx.doi.org/10.5194/angeo-24-1113-2006.
Simon, S., Kriegel, H., Saur, J., Wennmacher, A., Neubauer, F.M., Roussos, E., Motschmann, U., Dougherty, M.K., 2012. Analysis of Cassini magnetic field observations over the poles of Rhea. J. Geophys. Res. 117 (A16), 7211. http://dx.doi.org/10.1029/2012JA017747.
Simon, S., Saur, J., Neubauer, F.M., Motschmann, U., Dougherty, M.K., 2009. Plasma Wake of Tethys: hybrid simulations versus Cassini MAG data. Geophys. Res. Lett. 36, 4108. http://dx.doi.org/10.1029/2008GL036943.
Siscoe, G.L., Crooker, N.U., Erickson, G.M., Sonnerup, B.U.Ö., Siebert, K.D., Weimer, D.R., White, W.W., Maynard, N.C., 2000. Global geometry of magnetospheric currents inferred from MHD simulations. Wash. DC Am. Geophys. Union Geophys. Monogr. Ser. 118, 41.
Siscoe, G.L., Siebert, K.D., 2006. Bimodal nature of solar wind magnetosphere ionosphere thermosphere coupling. J. Atmos. Sol.-Terr. Phys. 68, 911–920. http://dx.doi.org/10.1016/j.jastp.2005.11.012.
Umeda, T., 2012. Effect of ion cyclotron motion on the structure of wakes: a Vlasov simulation. Earth Planets Space 64, 231–236.
Vasyliunas, V., 2006. Physical Origin of Pickup Currents. In: European Planetary Science Congress, Vol. 150.
Vernisse, Y., Kriegel, H., Wiehle, S., Motschmann, U., Glassmeier, K.-H., 2013. Stellar winds and planetary bodies simulations: lunar type interaction in Super-Alfvénic and Sub-Alfvénic flows. Planet. Space Sci. 84, 37–47. http://dx.doi.org/10.1016/j.pss.2013.04.004.
Wang, Y.-C., Mueller, J., Ip, W.-H., Motschmann, U., 2011. A 3D hybrid simulation study of the electromagnetic field distributions in the lunar wake. Icarus 216, 415–425. http://dx.doi.org/10.1016/j.icarus.2011.09.021.
Wang, Y.-C., Mueller, J., Motschmann, U., Ip, W.-H., 2010. A hybrid simulation of Mercury's magnetosphere for the MESSENGER encounters in year 2008. Icarus 209, 46–52. http://dx.doi.org/10.1016/j.icarus.2010.05.020.
Whang, Y.C., 1968. Interaction of the magnetized solar wind with the Moon. Phys. Fluids 11, 969–975. http://dx.doi.org/10.1063/1.1692068.
Wiehle, S., Plaschke, F., Motschmann, U., Glassmeier, K.-H., Auster, H.U., Angelopoulos, V., Mueller, J., et al., 2011. First lunar wake passage of ARTEMIS: discrimination of wake effects and solar wind fluctuations by 3D hybrid simulations. Planet. Space Sci. 59, 661–671. http://dx.doi.org/10.1016/j.pss.2011.01.012.
Wurz, P., Rohner, U., Whitby, J.A., Kolb, C., Lammer, H., Dobnikar, P., Martín-Fernández, J.A., 2007. The lunar exosphere: the sputtering contribution. Icarus 191, 486–496. http://dx.doi.org/10.1016/j.icarus.2007.04.034.
Yamauchi, M., Hara, T., Lundin, R., Dubinin, E., Fedorov, A., Sauvaud, J.-A., Frahm, R.A., et al., 2015. Seasonal variation of martian pick-up ions: evidence of breathing exosphere. Planet. Space Sci. 119, 54–61. http://dx.doi.org/10.1016/j.pss.2015.09.013.
Zhang, H., Khurana, K.K., Kivelson, M.G., Angelopoulos, V., Wan, W.X., Liu, L.B., Zong, Q.-G., Pu, Z.Y., Shi, Q.Q., Liu, W.L., 2014. Three-dimensional lunar wake reconstructed from ARTEMIS data. J. Geophys. Res. (Space Phys.) 119, 5220–5243. http://dx.doi.org/10.1002/2014JA020111.
Zhang, T.L., Luhmann, J.G., Russell, C.T., 1991. The magnetic barrier at Venus. J. Geophys. Res. 96, 11. http://dx.doi.org/10.1029/91JA00088.